PCCP

Accepted Manuscript

ROYAL SOCIETY OF CHEMISTRY

www.rsc.org/pccp

Physical Chemistry Chemical Physics
CREATED USING THE RSC LaTeX PCCP ARTICLE TEMPLATE – SEE www.rsc.org/electronicfiles FOR DETAILS
ARTICLE TYPE www. rsc.org/xxxxxx | XXXXXXXX

Mechanical properties and stabilities of α-Boron monolayers

Qing Peng[1,*], Liang Han[1], Xiaodong Wen [2,3], Sheng Liu[4], Zhongfang Chen[5], Jie Lian[1], and Suvranu De[1]

Received Xth XXXXXXXXXX 20XX, Accepted Xth XXXXXXXXX 20XX
First published on the web Xth XXXXXXXXXX 200X
DOI: 10.1039/C3RA41347K

We investigate the mechanical properties and stabilities of planar α-Boron monolayers under various large strains using density functional theory (DFT). The α-Boron has a high in-plane stiffness, about 2/3 of that of graphene, which suggest that α-Boron is four times as strong as iron. The potential profiles and the stress-strain curves indicate that the free standing α-Boron monolayer can sustain large tensile strains, up to 0.12, 0.16, and 0.18 for *armchair*, *zigzag*, and *biaxial* deformations, respectively. The third, fourth, and fifth order elastic constants are indispensable for accurate modeling of the mechanical properties under strains larger than 0.02, 0.06, and 0.08 respectively. The second order elastic constants, including in-plane stiffness, are predicted to monotonically increase with pressure, while the trend of Poisson ratio is reversed. The surface sound speeds of both compressional and shear waves increase with pressure. The ratio of these two sound speeds increases with the increase of pressure and converges to a value of 2.5. Our results imply that α-Boron monolayers are mechanically stable under various large strains with advanced mechanical properties–high strength and high flexibility.

1 INTRODUCTION

Similar to the element of carbon, boron has diverse forms of low-dimensional allotropic structures, predicted theoretically [1–18] and observed in experiments [19–24]. The 2D structure of the boron monolayer is especially interesting since the planar structure serves as the building block of 0D structures (flullerenes) by wrapping, 1D structures (nanotubes) by rolling, 3D structures (bulk) by stacking [25]. To the authors' best knowledge, the exact atomic structure of the boron monolayer sheet has not been determined from experiments, except an indirect evidence of the interlayer distance within multi-walled boron nanotubes (MWBNTs) being 3.2 Å [26]. On the contrary, various crystalline structures of monolayer structures of boron are predicted from *ab initio* computations, including α- [8,27–29], β- [27,28], γ- [3,27], $g_{1/8}$-, and $g_{2/15}$-sheets [9]. Distinctly different in structure, they all lie in a rather narrow range of vacancy concentrations of 10-15%. A first-principles-based global research of lowest-energy structures of the 2D boron sheets concludes that α sheets (Fig. 1) is the leading candidates [10,27,28,30]. Thus, we only focus on the α-Boron monolayers in this study.

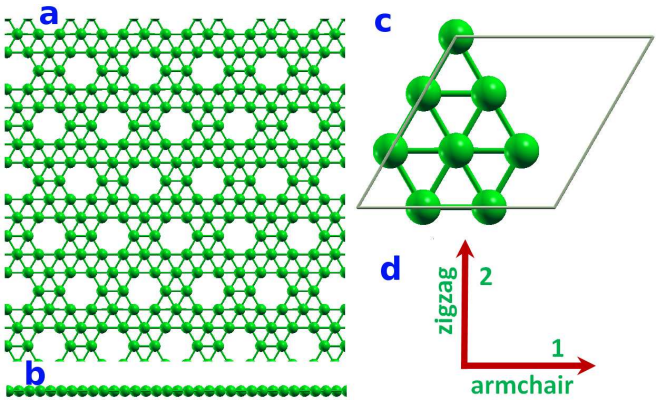

Fig. 1 Geometry and structure (a) Top-view and (b) side-view of the α-Boron monolayer plane; (c) the unit cell with simulation box and boron atoms; (d) the orientations of the system.

All the 2D Boron monolayer structures are determined by the ground-state energy minimization, which however ignores the profiles of the potential wells. In other words, the stability of the structure under disturbance is unknown. In addition, it is desired to know the mechanical properties of Boron 2D monolayer for three reasons. First, it is critical in designing parts or structures regarding their practical applications [31]. For instance, the application in the high-end bendable electronics requires the integration of the boron 2D monolayers with stretchable polymer substrates. Second, strain engineering is a common and important approach to tailor the functional and

[1] Address:Department of Mechanical, Aerospace and Nuclear Engineering, Rensselaer Polytechnic Institute, Troy, NY 12180, U.S.A.
[2] Address:State Key Laboratory of Coal Conversion, Institute of Coal Chemistry, Chinese Academy of Sciences, Taiyuan, China, 030001
[3] Address:Synfuels China Co. Ltd. Huairou, Beijing, China, 101407
[4] Address:School of Power and Mechanical Engineering, Wuhan University, Wuhan, China, 430072
[5] Address:Department of Chemistry, Institute for Functional Nanomaterials, University of Puerto Rico, Rio Piedras Campus, San Juan, PR 00931, U.S.A
[*] *E-mail* Qing Peng: qpeng.org@gmail.com

structural properties including bandgaps[32] and radiation hardness[33] of nanomaterials[34,35]. At last, nanomaterials is vulnerable to strain with or without intent because of its monatomic thickness[36,37]. For instance, there are strains because of the mismatch of lattice constants. In addition, elastic limits and tolerances are desirable for functional manipulation[38].

The goal of this paper is to study the mechanical stabilities and properties of α-Boron sheets, the leading lowest-energy Boron 2D monolayer structures. We used *ab initio* density functional theory calculations to model their responses under various mechanical loadings. The total energies of the system, forces on each atom, and stresses on the simulation boxes are directly obtained from DFT calculations. The response of the Boron 2D monolayers under the nonlinear deformation and fracture is studied, including ultimate strength and ultimate strain. The high order elastic constants are obtained by fitting the stress-strain curves to analytical stress-strain relationships that belong to the continuum formulation[39]. Based on our result of the high order elastic constants, the pressure dependent properties, such as sound speeds and the second order elastic constants, including the in-plane stiffness, are predicted. Our results are compared to that of graphene, graphene-like Boron Nitride (g-BN), and graphene-like silicon monolayers g-Si. The results of graphene[40], g-BN[39] and g-Si[41] were reported previously. Because these three structures are experimentally fabricated, well known, and well studied, they can serve as a reference to α-Boron sheets as they have similar structures. Our results for the continuum formulation could also be useful in finite element modeling of the multi-scale calculations for mechanical properties of Boron 2D monolayer at the continuum level[42]. The organization of this paper is as follows. Section II presents the computational details of DFT calculations. The results and analysis are in section III, followed by conclusions in section IV.

2 DENSITY FUNCTIONAL THEORY CALCULATIONS

The structures of monolayer α-Boron are explicitly examined in this study because α-Boron is the first leading candidates for the lowest energy structures[10,27,28]. As convention, we define the *armchair* direction as the nearest neighbor direction and the *zigzag* direction is perpendicular to it within the atomic plane formed by nearest neighbors. The periodic boundary conditions along the plane are applied. The total energies of the system, forces on each atom, stresses, and stress-strain relationships of boron 2D monolayers under the desired deformation configurations are characterized via DFT. The calculations were carried out with the Vienna Ab-initio Simulation Package (VASP)[43,44] which is based on the Kohn-Sham Density Functional Theory (KS-DFT)[45] with the generalized gradient approximations as parameterized by Perdew, Burke, and Ernzerhof (PBE) for exchange-correlation functions[46] since it was reported to be reliable in modeling Boron nanomaterials[47]. The electrons explicitly included in the calculations are the $2s^2 2p^1$ electrons for boron atoms. The core electrons are replaced by the projector augmented wave (PAW) and pseudopotential approach[48]. A plane-wave cutoff of 500 eV is used in all the calculations. The convergence of the total energy and forces is 10^{-5} eV and 10^{-3} eV/Å, respectively. The calculations are performed at zero temperature.

The atomic structures of all the deformed and undeformed configurations were obtained by fully relaxing a 9-atom-unit cell where all atoms were placed in one plane. The simulation invokes periodic boundary conditions for the two in-plane directions. There is a 15 Å thick vacuum region to reduce the inter-layer interaction to model the single layer system. To eliminate the artificial effect of the out-of-plane thickness of the simulation box on the stress, we use the the second Piola-Kirchhoff stress[39] to express the 2D forces per length with units of N/m.

All of the boron sheets can be constructed by carving different patterns of hexagonal holes within the triangular sheet. The perfect triangle sheet has the atomic lattice point group D_{3h}. For a general deformation state, the number of independent components of the second, third, fourth, and fifth order elastic tensors are 21, 56, 126, and 252 respectively. However, there are only fourteen independent elastic constants that need to be explicitly considered due to the symmetries of the atomic lattice point group D_{3h}, which consists of a three-fold rotational axis and three mirror planes.

The fourteen independent elastic constants of 2D boron are determined by a least-squares fit to the stress-strain results from DFT calculations in two steps, detailed in our previous work[39], which had been well used to explore the mechanical properties of 2D materials[40,41,49–58]. A brief introduction is that, in the first step, we use a least-squares fit of five stress-strain responses. Five relationships between stress and strain are necessary because there are five independent fifth-order elastic constants (FFOEC). We obtain the stress-strain relationships by simulating the following deformation states: uniaxial strain in the zigzag direction (*zigzag*); uniaxial strain in the armchair direction (*armchair*); and equibiaxial strain (*biaxial*). From the first step, the components of the second-order elastic constants (SOEC), the third-order elastic constants (TOEC), and the fourth-order elastic constants (FOEC) are over-determined (i.e, the number of linearly independent variables are greater than the number of constrains), and the fifth-order elastic constants are well-determined (the number of linearly independent variables are equal to the number of constrains). Under such circumstances, the second step is needed: least-square solution to these over- and well- determined linear equations.

3 RESULTS AND ANALYSIS

3.1 Atomic structure

Previous studies show that α-sheet is a leading candidate for the most stable planar (or locally unbuckled) boron sheet[10,27,28] . A special structural feature of α-sheet is that every center-occupied hexagon is isolated from each other. The α-Boron sheets are perfectly flat, as illustrated from the side-view of the plane in Fig. 1(b), and we pay special attention to this structure in this study.

We first optimized the geometry of the unit cells of the α-Boron monolayer which contains eight boron atoms. The most energetically favorable structure is set as the strain-free structure in this study. The optimized atomic structures, as well as the conventional cells are shown in Fig. 1. Our atomic structure is in good agreement with previous DFT calculations.

3.2 Energy Profile

When strain is applied, the system will be disturbed away from the equilibrium state. Since the configuration energy of the strain-free configuration is the minima of the potential well, any strain will increase the system's energy. By applying different amounts of strain along different directions, the potential well can be explored. Once the strain is applied, all the atoms of the system are allowed full freedom of motion. A quasi-Newton algorithm is used to relax all atoms into equilibrium positions within the deformed unit cell that yields the minimum total energy for the imposed strain state of the super cell.

Both compression and tension are considered with Lagrangian strains ranging from -0.1 to 0.3 with an increment of 0.02 in each step for all three deformation modes. It is important to include the compressive strains since they are believed to be the cause of the rippling of the free standing atomic sheet[59]. It was observed that a graphene sheet experiences biaxial compression after thermal annealing[60], which could also happen with Boron 2D monolayers. Such an asymmetrical range was chosen due to the non-symmetric mechanical responses of material, as well as its mechanical instability[61], to the compressive and the tensile strains, as illustrated in the next subsection.

We define the strain energy per atom $E_s = (E_{tot} - E_0)/n$, where E_{tot} is the total energy of the strained system, E_0 is the total energy of the strain-free system, and $n = 8$ is the number of atoms in the unit cell. This size-independent quantity is used for comparison between different systems. The E_s of the α-Boron monolayer as a function of strain in uniaxial armchair, uniaxial zigzag, and biaxial deformation are plotted in Fig. 2a. The result of the potential profile of α-Boron is compared with that of graphene (Fig. 2b) and g-BN (Fig. 3c). E_s is anisotropic with strain direction. E_s is non-symmetrical for

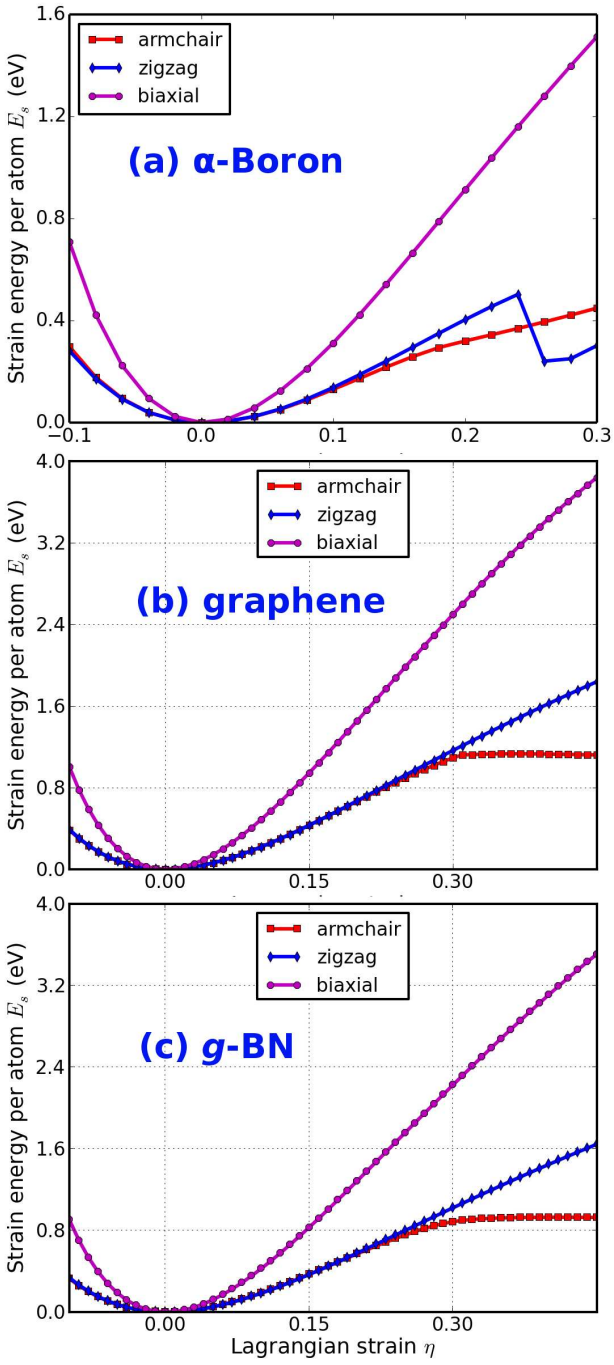

Fig. 2 Energy profile The strain energy per atom under uniaxial strain in armchair and zigzag directions, and equibiaxial strains of α-Boron (a), compared with graphene (b) and g-BN (c).

compression (η <0) and tension (η >0) for all three modes. This non-symmetry indicates the anharmonicity of the Boron 2D monolayer structures. The harmonic region where the E_s is a quadratic function of applied strain can be taken between -0.02< η <0.02. The stresses, derivatives of the strain energies, are linearly increasing with the increase of the applied strains in the harmonic region.

The anharmonic region is the range of strain where the linear stress-strain relationship is invalid and higher order terms are not negligible. With even larger loading of strains, the systems will undergo irreversible structural changes, and the systems are in a plastic region where they may fail. The maximum strain in the anharmonic region is the *critical* strain. The critical strain under uniaxial armchair, uniaxial zigzag, and biaxial deformation is $\eta_c^a = 0.30$, $\eta_c^z = 0.24$, and $\eta_c^b = 0.30$, respectively. The width of the stable region is the opening width of the potential energy well (Fig. 2). The opening width of the potential energy well η_s could serve as a scale to quantify the stability of nano structures. Thus the average width of the stable regions of the three deformation modes (i.e., the opening width of the potential energy wells) is a reasonably good scale for the mechanical stabilities of the nano structures, denoted as η_s. As a result, from the point view of potential energy, we conclude that α-Boron is mechanically stable. However, it is less stable than graphene and *g*-BN as expected.

The ultimate strains are determined as the corresponding strain of the ultimate stress, which is the maxima of the stress-strain curve, as discussed in the following section. Note that in general the compressive strains will cause rippling of the *free-standing* thin films, membranes, plates, and nanosheets[59]. The critical compressive strain for rippling instability is much less than the critical tensile strain for fracture, for example, 0.0001% versus 2% in graphene sheets[61]. However, the rippling can be suppressed by applying constraints, such as embedding (0.7%)[62], substrates (0.4% before heating)[60], thermal cycling on SiO_2 (0.05%)[63] and BN (0.6%)[64], and sandwiching[65]. Our study of compressive strains is important in understanding the mechanics of these non-rippling applications. The rippling phenomena are interesting and important, which is, however, out the scope of this study.

3.3 Stress-strain relationships

The second P-K stress versus Lagrangian strain relationships of α-Boron sheets for uniaxial strains along the armchair and zigzag directions, as well as biaxial strains, are shown in Fig. 3a, compared with that of graphene (Fig. 3b) and *g*-BN (Fig. 3c), since these two nano materials were extensively studied and well known. The results show that the α-Boron sheets can sustain large strains. The ultimate tensile strength is the maximum stress that a material can withstand while being stretched, and the corresponding strain is the ultimate strain.

Table 1 Elastic limits Ultimate strengths (Σ_m^a,Σ_m^z,Σ_m^b) in units of N/m and ultimate strains (η_m^a, η_m^z, η_m^b) under uniaxial strain (armchair and zigzag) and biaxial from DFT calculations, compared with graphene, *g*-BN, and *g*-Si.

	α-Boron	Graphene[a]	*g*-BN[b]	*g*-Si[c]
Σ_m^a	12.8	28.6	23.6	6.3
η_m^a	0.12	0.19	0.18	0.15
Σ_m^z	16.0	30.4	26.3	6.0
η_m^z	0.16	0.23	0.26	0.16
Σ_m^b	18.1	32.1	27.8	6.3
η_m^b	0.18	0.23	0.24	0.15

[a] Ref.[40];
[b] graphene-like Boron nitride monolayer from Ref.[39];
[c] graphene-like silicon monolayer from Ref.[57];

Under ideal conditions, the critical strain is larger than the ultimate strain. The systems of perfect α-Boron sheets under strains beyond the ultimate strains are in a meta-stable state. The ultimate tensile strain, which reflects the intrinsic bonding strengths and acts as a lower limit of the critical strain, should be considered when exploring the potential applications.

The ultimate tensile strains of α-Boron sheets are 0.12, 0.16, and 0.18 along the armchair, zigzag, and biaxial, respectively (Table 1). The ultimate tensile stresses are 12.8, 16.0, and 18.1 N/m for the armchair, zigzag, and biaxial strains, respectively. The α-Boron sheets exhibits a large ultimate tensile stress of 18.1 N/m, which is about 56.6 GPa if we take the monolayer height of 3.2 Å [26]. Such a large ultimate tensile stress could serve as an another evidence of its stability and bond strengths.

The ultimate strengths and strains corresponding to the different strain conditions are summarized in Table 1, compared with that of graphene, *g*-BN, and planar silicene (*g*-Si). since they have similar structure and they are close to each other in the periodic table. The α-Boron sheet behaves in an asymmetric manner with respect to compressive and tensile strains. With increasing strains, the B-B bonds are stretched and eventually rupture. The positive slope of the stress-strain curves and the positive ultimate tensile stresses indicate that this structure is mechanical stable. The α-Boron has smaller ultimate tensile strengths than graphene and *g*-BN, but larger than *g*-Si. This indicates that α-Boron will have a better mechanical performance than *g*-Si which had been fabricated, but worse than graphene and *g*-BN as expected.

We examined the elastic stability under pure shearing along the armchair direction. The stress-strain relationship is shown in Fig. 4. The α-Boron monolayers are stable in the examined range of shearing as of -0.1 to 0.2.

Our results show that the α-Boron sheet has good me-

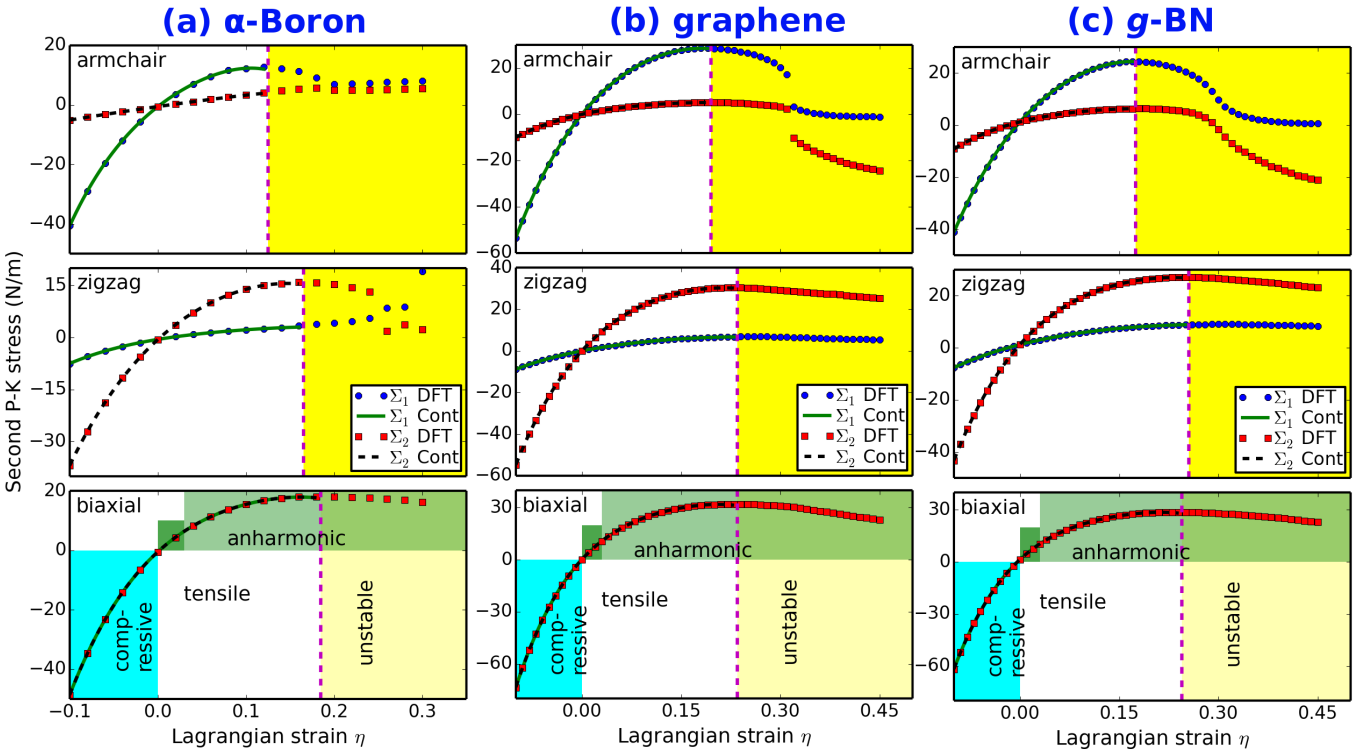

Fig. 3 Stress-strain responses The stress-strain relationships of the α-Boron monolayers under the armchair, zigzag, and biaxial strains. Σ_1 (Σ_2) denotes the x (y) component of stress. "Cont" stands for the fitting of DFT calculations ("DFT") to continuum elastic theory. The compressive domain is $\eta < 0$ (cyan) and the tensile domain is $\eta > 0$ (green). The harmonic region is $\eta \leq \eta_h$ and the anharmonic region is $\eta_h < \eta \leq \eta_m$. The mechanically unstable region is $\eta > \eta_m$ (yellow region), and the mechanically stable region is $\eta \leq \eta_m$.

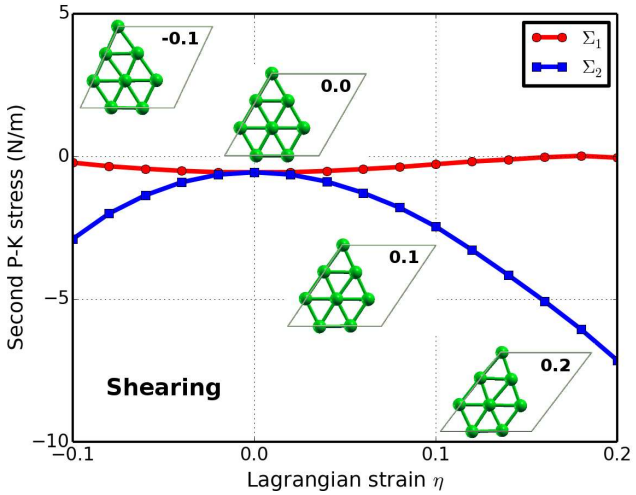

Fig. 4 Shearing The stress-strain relationships of the α-Boron monolayers under pure shearing along the armchair direction. Σ_1 (Σ_2) denotes the x (y) component of stress. The insets are the snapshots of the configurations under different shearing state.

chanical performance under various strains. The stress-strain curves indicate that the α-Boron sheet is a stable structure under mechanical strains. Recall that the potential wells of α-Boron sheet are also wide open with high instability barriers (Fig. 2). Our results are consistent with previous highly accurate PBE0 calculations which concluded that the α-Boron sheet has largest cohesive energy and dynamical stabilities from phonon calculations [10].

Note that the softening of the Boron 2D monolayers under strains beyond the ultimate strains only occurs for ideal conditions. The systems under this circumstance are in a metastable state, which can be easily destroyed by long wavelength perturbations and vacancy defects, as well as high temperature effects, and enter a plastic state [66]. Thus only the data within the ultimate strain has physical meaning and was used in determining the high order elastic constants in the following subsection.

3.4 Elastic Constants

The elastic constants are critical parameters in finite element analysis models for mechanical properties of materials [42]. Our results of these elastic constants provide an accurate continuum description of the elastic properties of Boron 2D monolayers from *ab initio* density functional theory calculations. They are suitable for incorporation into numerical methods such as the finite element technique.

The second order elastic constants model the linear elastic response. The higher (> 2) order elastic constants are important to characterize the nonlinear elastic response of Boron 2D monolayers using a continuum description. These can be obtained using a least squares fit of the DFT data and are reported in Table 2. Corresponding values for graphene are also shown.

The in-plane Young's modulus Y_s (or stiffness) and Poison's ratio ν may be obtained from the following relationships: $Y_s = (C_{11}^2 - C_{12}^2)/C_{11}$ and $\nu = C_{12}/C_{11}$. For α Boron sheet, we have Y_s =224.6 N/m, and ν =0.165. The in-plane stiffness is smaller (about 2/3) than that of graphene (341 N/m [40]), and g-BN (278.3 N/m [39]) however it is still relatively large compared to metals. Taken the experimental value of 3.2 Å as the height of Boron 2D monolayer [26]. This stiffness is equivalent to 702 GPa, which is relatively strong – about 4 times of the strength of iron, recalling that the stiffness of iron is about 170 GPa. Although the α-Boron sheet is less stiff than graphene and g-BN, it is much stronger than g-Si. The Poisson ratio of α-Boron sheet is very close to that of graphene, but much smaller than g-BN and g-Si, indicating less shear motion in α-Boron under strains.

Besides second order elastic constants, higher order (> 2) elastic constants are also important quantities. [67–69] Experimentally by measuring the changes of sound velocities under the application of hydrostatic and uniaxial stresses, these high order elastic constants can be determined [70,71]. The high order elastic constants are very important in studying the nonlinear elasticity [72], thermal expansion (through gruneisen parameter) [73], temperature dependence of elastic constants [73,74], harmonic generation [71], phonon-phonon interactions [75], photon-phonon interactions [76], lattice defects [77], phase transitions [78], echo phenomena [79], and strain softening [80], and so on [40]. In addition, with the higher order elastic continuum description utilizing these elastic constants, one can model the stress and deformation state under uniaxial stress, rather than uniaxial strain [81]. Explicitly, when pressure is applied, the pressure dependent second-order elastic moduli can be obtained from the high order elastic continuum description [39]. The third-order elastic constants are important in understanding the nonlinear elasticity of materials, such as changes in acoustic velocities due to finite strain. As a consequence, nano devices (such as nano surface acoustic wave sensors and nano waveguides) could be synthesized by introducing local strain [31,49], as discussed in details later in this paper.

Stress-strain curves in the previous section show that they will soften when the strain is larger than the ultimate strain. From the view of electron bonding, this is due to the bond weakening and breaking. This softening behavior is determined by the TOECs and FFOECs in the continuum aspect. The negative values of TOECs and FFOECs ensure the softening of Boron 2D monolayer under large strain.

A good way to check the importance of the high order elastic constants is to consider the case when they are missing. With the elastic constants, the stress-strain response can be predicted from elastic theory [39]. When we only consider the second order elasticity, the stress varies with strain linearly.

Table 2 Elastic constants Nonzero independent components for the SOEC, TOEC, FOEC, and FFOEC tensor components, Poisson's ratio ν and in-plane stiffness Y_s of α-Boron monolayers from DFT calculations, compared with graphene, g-BN, and g-Si.

		α-Boron	Graphene[a]	g-BN[b]	g-Si[c]
a (Å)		3.865	2.468	2.512	3.901
Y_s (N/m)		224.6	340.8	278.3	71.2
ν		0.165	0.178	0.225	0.401
SOECs	C_{11} (N/m)	230.9	352.0	293.2	84.8
	C_{12} (N/m)	38.0	62.6	66.1	34.1
TOECs	C_{111} (N/m)	-2126.6	-3089.7	-2513.6	-696.5
	C_{112} (N/m)	-318.9	-453.8	-425.0	-281.6
	C_{222} (N/m)	-2373.6	-2928.1	-2284.2	-617.2
FOECs	C_{1111} (N/m)	10987	21927	16547	1951
	C_{1112} (N/m)	480	2731	2609	1683
	C_{1122} (N/m)	2912	3888	2215	2549
	C_{2222} (N/m)	18768	18779	12288	1108
FFOECs	C_{11111} (N/m)	-44814	-118791	-65265	-19595
	C_{11112} (N/m)	-92368	-19173	-8454	-11405
	C_{11122} (N/m)	-58393	-15863	-28556	-7628
	C_{12222} (N/m)	-70897	-27463	-36955	-16955
	C_{22222} (N/m)	-435594	-134752	-100469	-21326

[a] Ref.[40];
[b] graphene-like Boron nitride monolayer from Ref.[39];
[c] graphene-like silicon monolayer from Ref.[57];

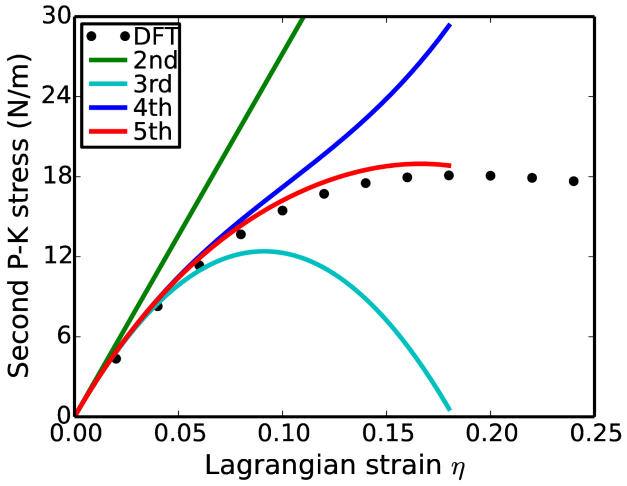

Fig. 5 Order effects The predicted stress-strain responses of biaxial deformation of ordered graphene oxide monolayer from different orders (second, third, fourth, and fifth order) of elastic constants of α-Boron sheet, compared to that from the DFT calculations (circle line), using biaxial deformation as an example.

Here we take the biaxial deformation of the α-Boron sheet as an example. As illustrated in Fig. 5, the linear behaviors are only valid within a small strain range, about $-0.02 \leq \eta \leq 0.02$, as the same result obtained from the energy versus strain curves in Fig. 2. With the knowledge of the elastic constants up to the third order, the stress-strain curve can be accurately predicted within the range of $-0.04 \leq \eta \leq 0.04$. Using the elastic constants up to the fourth order, the mechanical behaviors can be well treated up to a strain as large as 0.08. For the strains beyond 0.08, the fifth order elastic are required for an accurate modeling. The analysis of the uniaxial deformations comes to the similar results.

Our results illustrate that the monatomic layer structures possess different mechanical behaviors in contrast to the bulk or multi-layered structures, where the second order elastic constants are sufficient in most cases. The second order elastic constants are relatively easier to be calculated from the strain energy curves[66,82], however, they are not sufficient for monatomic layer structures. The high order elastic constants are required for an accurate description of the mechanical behaviors of monatomic layer structures since they are vulnerable to strain due to the geometry confinements.

Our results of mechanical properties of Boron 2D monolayers are limited to zero temperature due to current DFT calculations. Once finite temperatures are considered, the thermal

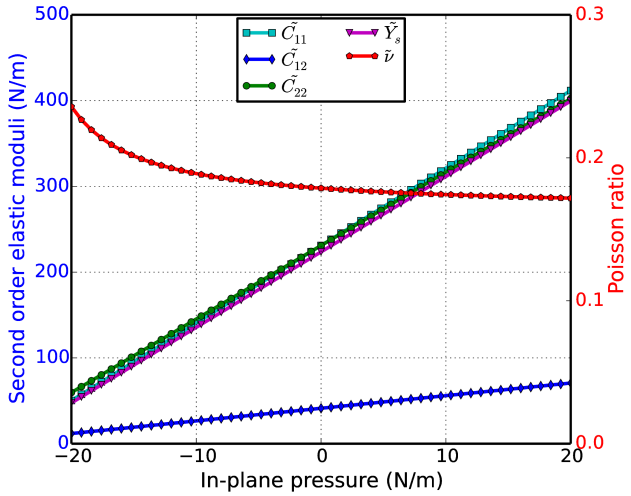

Fig. 6 Pressure dependent elastic moduli Second-order elastic moduli and Poisson ratio as function of the pressure for the α-Boron monolayer from DFT predictions.

expansions and dynamics will in general reduce the interactions between atoms. As a result, the longitudinal mode elastic constants will decrease with respect to the temperature of the system. The variation of shear mode elastic constants should be more complex in responding to the temperature. A thorough study will be interesting, which is, however, beyond the scope of this study.

3.5 Pressure effect on the elastic moduli

With third-order elastic moduli, one can study the effect of the second-order elastic moduli on the pressure p acting in the plane of Boron 2D monolayers. Explicitly, when pressure is applied, the pressure dependent second-order elastic moduli ($\tilde{C}_{11}, \tilde{C}_{12}, \tilde{C}_{22}$) can be obtained from $C_{11}, C_{12}, C_{22}, C_{111}, C_{112}, C_{222}, Y_s$, and ν as[53–55]:

$$\tilde{C}_{11} = C_{11} - (C_{111} + C_{112})\frac{1-\nu}{Y_s}P, \quad (1)$$

$$\tilde{C}_{22} = C_{11} - C_{222}\frac{1-\nu}{Y_s}P \quad (2)$$

$$\tilde{C}_{12} = C_{12} - C_{112}\frac{1-\nu}{Y_s}P \quad (3)$$

The general trend is that the second-order elastic moduli increase linearly with the applied pressure (Fig. 6). $\tilde{C}_{11}$ is asymmetrical to $\tilde{C}_{22}$ unlike the zero pressure case. $\tilde{C}_{11} = \tilde{C}_{22} = C_{11}$ only occurs when the pressure is zero. This anisotropy could be the outcome of anharmonicity. The Fig. 6 depicts the general trend that Poisson's ratio decreases monotonically with the increase of pressure. Our results show that the α-Boron sheet are mechanically stable under the various pressures.

3.6 Pressure effect on the velocities of sound

As shown in previous subsections, there are non-zero in-plane Young's moduli and shear deformations in the α-Boron monolayers. These mechanical properties could have important applications. Specifically, it is possible to generate sound waves with different velocities depending on the deformation mode. Sound waves generating biaxial deformations (compressions) are compressional or p-waves. Sound waves generating shear deformations are shear or s-waves. The sound velocities of these two types of waves are calculated from the second-order elastic moduli and mass density using the following relations:

$$v_p = \sqrt{\frac{\tilde{Y}_s(1-\tilde{\nu})}{\rho_m(1+\tilde{\nu})(1-2\tilde{\nu})}}, \quad (4)$$

$$v_s = \sqrt{\frac{\tilde{C}_{12}}{\rho_m}}. \quad (5)$$

The dependence of v_p and v_s on pressure (biaxial stress) is plotted in Fig. 7. Both v_p and v_s monotonically increase with an increase in pressure. Thus they can be tuned by introducing the biaxial strain through the stress-strain relationship shown in Fig. 3.

The ratio of the compressional to shear wave velocities (v_p/v_s) is a very useful parameter in the determination of a material's mechanical properties. It depends only on the Poisson's ratio as

$$\frac{v_p}{v_s} = \sqrt{\frac{1}{\tilde{\nu}}(1+\frac{\tilde{\nu}^2}{1-2\tilde{\nu}})}. \quad (6)$$

The ratio of v_p/v_s decreases with the increase of pressure (Fig. 7), and it approaches a value of 2.5 at positive pressure.

As shown in Fig. 7, a sound velocity gradient could be achieved by introducing stress into an α-Boron monolayer. such a sound velocity gradient could lead to refraction of sound wavefronts in the direction of lower sound speed, causing the sound rays to follow a curved path[83]. The radius of curvature of the sound path is inversely proportional to the gradient. Such a negative sound speed gradient could also be achieved by a negative strain gradient. This tunable sound velocity gradient can be used to form a sound frequency and ranging channel, which is the functional mechanism of waveguides and surface acoustic wave (SAW) sensors[84–86]. Counting on the large ultimate tensile strengths, α-Boron-based nano-devices of SAW sensors, filters, and waveguides might be synthesized using local strains for next generation electronics.

4 CONCLUSIONS

In summary, by applying various mechanical strains, we studied the mechanical properties and stabilities of the α-Boron

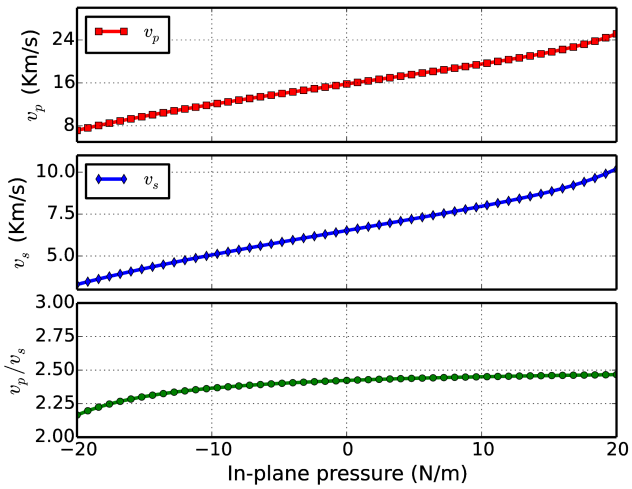

Fig. 7 Sound velocity p-wave and s-wave velocities, and compressional to shear wave velocity ratio v_p/v_s as a function of in-plane pressure.

monolayer. The potential profiles, the stress-strain relationships, the in-plane stiffness, Poisson's ratio, second order, third order, fourth order, and fifth order elastic constants, the ultimate stresses, ultimate strains, critical strains, and the pressure effect on the elastic moduli are studied. According to the results of the positive ultimate strengths and strains, second order elastic constants, and the in-plane Young's modulus, we conclude that α-Boron structures are mechanically stable under various strains and pressures.

The nonlinear elasticity of the structure is also investigated. We obtained an accurate continuum description of the elastic properties of this structure by explicitly determining the fourteen independent components of high order (up to fifth order) elastic constants from the fitting of stress-strain curves obtained from DFT calculations. This data is useful to develop a continuum description which is suitable for incorporation into a finite element analysis model for its applications at large scale. We also determined the valid range using these elastic constants in different orders. The harmonic elastic constants are only valid with a small range of -0.02 $\leq \eta \leq$ 0.02. With the knowledge of the elastic constants up to the third order, the stress-strain curve can be accurately predicted within the range of -0.06 $\leq \eta \leq$ 0.06. Using the elastic constants up to the fourth order, the mechanical behaviors can be accurately predicted up to a strain as large as 0.08. For the strains beyond 0.08, the fifth order elastic constants are required for accurate modeling. The high order elastic constants reflect the high order nonlinear bond strength under large strains.

We predicted that both the second order elastic constants and the in-plane stiffness monotonically increase with elevating pressure, while the trend of Poisson ratio is reversed. The sound velocity of both compressional and shear waves increase with pressure. The ratio of v_p/v_s decreases with the increase of pressure and converges to a value of 2.5 at positive pressure. Our results could serve as a road map for the synthesis of the α-Boron monolayers.

ACKNOWLEDGEMENTS

We thank Xiaojun Wu for helpful discussions. The authors would like to acknowledge the generous financial support from the Defense Threat Reduction Agency (DTRA) Grant # BRBAA08-C-2-0130 and # HDTRA1-13-1-0025, and a NSF Career award under the Award number of DMR 1151028. Support by Department of Defense (Grant W911NF-12-1-0083) is gratefully acknowledged by Z.C.

References

1 I. Boustani, *Surf. Sci.*, 1997, **370**, 355–363.
2 N. G. Szwacki, A. Sadrzadeh and B. I. Yakobson, *Phys. Rev. Lett.*, 2007, **98**, 166804.
3 C. Ozdogan, S. Mukhopadhyay, W. Hayami, Z. B. Guvenc, R. Pandey and I. Boustani, *J. Phys. Chem. C*, 2010, **114**, 4362–4375.
4 A. Ceulemans, J. T. Muya, G. Gopakumar and M. T. Nguyen, *Chem. Phys. Lett.*, 2008, **461**, 226 – 228.
5 H. Tang and S. Ismail-Beigi, *Phys. Rev. B*, 2009, **80**, 134113.
6 R. R. Zope, T. Baruah, K. C. Lau, A. Y. Liu, M. R. Pederson and B. I. Dunlap, *Phys. Rev. B*, 2009, **79**, 161403.
7 I. Boustani, Z. Zhu and D. Tománek, *Phys. Rev. B*, 2011, **83**, 193405.
8 T. R. Galeev, Q. Chen, J.-C. Guo, H. Bai, C.-Q. Miao, H.-G. Lu, A. P. Sergeeva, S.-D. Li and A. I. Boldyrev, *Phys. Chem. Chem. Phys.*, 2011, **13**, 11575–11578.
9 E. S. Penev, S. Bhowmick, A. Sadrzadeh and B. I. Yakobson, *NANO Lett.*, 2012, **12**, 2441–2445.
10 X. Wu, J. Dai, Y. Zhao, Z. Zhuo, J. Yang and X. C. Zeng, *ACS Nano*, 2012, **6**, 7443–7453.
11 X. Li, X. Wu, X. C. Zeng and J. Yang, *ACS Nano*, 2012, **6**, 4104–4112.
12 X. Wu, J. Dai, Y. Zhao, Z. Zhuo, J. Yang and X. C. Zeng, *ACS Nano*, 2013, **7**, 880–881.
13 I. A. Popov, Z. A. Piazza, W.-L. Li, L.-S. Wang and A. I. Boldyrev, *J. Chem. Phys.*, 2013, **139**, 144307.
14 Y. Liu, E. S. Penev and B. I. Yakobson, *Angew. Chem. Int. Ed.*, 2013, **52**, 3156–3159.
15 X.-F. Zhou, X. Dong, A. R. Oganov, Q. Zhu, Y. Tian and H.-T. Wang, *Phys. Rev. Lett.*, 2014, **112**, 085502.

16 W.-L. Li, Y.-F. Zhao, H.-S. Hu, J. Li and L.-S. Wang, *Angew. Chem. Int. Ed.*, 2014, **53**, 5540–5545.
17 H. Liu, J. Gao and J. Zhao, *Sci. Rep.*, 2013, **3**, 3238.
18 M. Amsler, S. Botti, M. A. L. Marques and S. Goedecker, *Phys. Rev. Lett.*, 2013, **111**, 136101.
19 H. Zhai, B. Kiran, J. Li and L. Wang, *Nat. Mater.*, 2003, **2**, 827–833.
20 H. Zhai, A. Alexandrova, K. Birch, A. Boldyrev and L. Wang, *Angew. Chem. Int. Ed.*, 2003, **42**, 6004–6008.
21 W. Huang, A. P. Sergeeva, H.-J. Zhai, B. B. Averkiev, L.-S. Wang and A. I. Boldyrev, *Nat. Chem.*, 2010, **2**, 202–206.
22 A. N. Alexandrova, A. I. Boldyrev, H.-J. Zhai and L.-S. Wang, *Coord. Chem. Rev.*, 2006, **250**, 2811–2866.
23 T. R. Galeev, Q. Chen, J.-C. Guo, H. Bai, C.-Q. Miao, H.-G. Lu, A. P. Sergeeva, S.-D. Li and A. I. Boldyrev, *Phys. Chem. Chem. Phys.*, 2011, **13**, 11575–11578.
24 Z. A. Piazza, H.-S. Hu, W.-L. Li, Y.-F. Zhao, J. Li and L.-S. Wang, *Nat. Commun.*, 2014, **5**, 3113.
25 A. H. Castro Neto, F. Guinea, N. M. R. Peres, K. S. Novoselov and A. K. Geim, *Rev. Mod. Phys.*, 2009, **81**, 109–162.
26 F. Liu, C. Shen, Z. Su, X. Ding, S. Deng, J. Chen, N. Xu and H. Gao, *J. Mater. Chem.*, 2010, **20**, 2197–2205.
27 H. Tang and S. Ismail-Beigi, *Phys. Rev. Lett.*, 2007, **99**, 115501.
28 H. Tang and S. Ismail-Beigi, *Phys. Rev. B*, 2010, **82**, 115412.
29 J. Miller, *Phys. Today*, 2007, **60**, 20–21.
30 X. Yu, L. Li, X.-W. Xu and C.-C. Tang, *J. Phys. Chem. C*, 2012, **116**, 20075–20079.
31 Q. Peng, A. R. Zamiri, W. Ji and S. De, *Acta Mechanica*, 2012, **223**, 2591–2596.
32 Q. Peng and S. De, *Physica E*, 2012, **44**, 1662–1666.
33 Q. Peng, W. Ji and S. De, *Nanoscale*, 2013, **5**, 695–703.
34 F. Guinea, M. I. Katsnelson and A. K. Geim, *Nat. Phys.*, 2010, **6**, 30–33.
35 M. Topsakal, S. Cahangirov, E. Bekaroglu and S. Ciraci, *Phys. Rev. B*, 2009, **80**, 235119.
36 Q. Peng, J. Crean, A. K. Dearden, X. Wen, C. Huang, S. P. A. Bordas and S. De, *Mod. Phys. Lett. B*, 2013, **27**, 1330017.
37 Q. Peng, A. K. Dearden, J. Crean, L. Han, S. Liu, X. Wen and S. De, *Nanotechn. Sci. Appl.*, 2014, **7**, 1–29.
38 Q. Peng and S. De, *Nanoscale*, 2014, **6**, 12071–12079.
39 Q. Peng, W. Ji and S. De, *Comput. Mater. Sci.*, 2012, **56**, 11 – 17.
40 Q. Peng, C. Liang, W. Ji and S. De, *Phys. Chem. Chem. Phys.*, 2013, **15**, 2003–2011.
41 Q. Peng and S. De, *RSC Adv.*, 2013, **3**, 24337 – 24344.
42 X. Wei and J. W. Kysar, *Int. J. Solids Struct.*, 2012, **49**, 3201 – 3209.
43 G. Kresse and J. Hafner, *Phys. Rev. B*, 1993, **47**, 558.
44 G. Kresse and J. Furthuller, *Comput. Mater. Sci.*, 1996, **6**, 15.
45 W. Kohn and L. J. Sham, *Phys. Rev.*, 1965, **140**, A1133.
46 J. P. Perdew, K. Burke and M. Ernzerhof, *Phys. Rev. Lett.*, 1996, **77**, 3865–3868.
47 F. Li, P. Jin, D.-e. Jiang, L. Wang, S. B. Zhang, J. Zhao and Z. Chen, *J. Chem. Phys.*, 2012, **136**, 074302.
48 R. O. Jones and O. Gunnarsson, *Rev. Mod. Phys.*, 1989, **61**, 689–746.
49 Q. Peng, W. Ji and S. De, *Phys. Chem. Chem. Phys.*, 2012, **14**, 13385–13391.
50 Q. Peng, C. Liang, W. Ji and S. De, *Model. Numer. Simul. Mater. Sci.*, 2012, **2**, 76–84.
51 Q. Peng, C. Liang, W. Ji and S. De, *Comput. Mater. Sci.*, 2013, **68**, 320–324.
52 Q. Peng, X.-J. Chen, S. Liu and S. De, *RSC Adv.*, 2013, **3**, 7083–7092.
53 Q. Peng, C. Liang, W. Ji and S. De, *Mech. Mater.*, 2013, **64**, 135–141.
54 Q. Peng, X.-J. Chen, W. Ji and S. De, *Adv. Eng. Mater.*, 2013, **15**, 718–727.
55 Q. Peng, C. Liang, W. Ji and S. De, *Appl. Phys. A*, 2013, **13**, 483–490.
56 Q. Peng, Z. Chen and S. De, *Mech. Adv. Mater. Struc.*, 2013, DOI:10.1080/15376494.2013.839067.
57 Q. Peng, X. Wen and S. De, *RSC Adv.*, 2013, **3**, 13772 – 13781.
58 Q. Peng and S. De, *Phys. Chem. Chem. Phys.*, 2013, **15**, 19427 – 19437.
59 E. Cerda and L. Mahadevan, *Phys. Rev. Lett.*, 2003, **90**, 074302.
60 W. Bao, F. Miao, Z. Chen, H. Zhang, W. Jang, C. Dames and C. N. Lau, *Nat. Nanotech.*, 2009, **4**, 562–566.
61 Y. Zhang and F. Liu, *Appl. Phys. Lett.*, 2011, **99**, 241908.
62 G. Tsoukleri, J. Parthenios, K. Papagelis, R. Jalil, A. C. Ferrari, A. K. Geim, K. S. Novoselov and C. Galiotis, *Small*, 2009, **5**, 2397–2402.
63 D. Yoon, Y.-W. Son and H. Cheong, *Nano Lett.*, 2011, **11**, 3227–3231.
64 W. Pan, J. Xiao, J. Zhu, C. Yu, G. Zhang, Z. Ni, K. Watanabe, T. Taniguchi, Y. Shi and X. Wang, *Sci. Rep.*, 2012, **2**, 893.
65 R. Quhe, J. Zheng, G. Luo, Q. Liu, R. Qin, J. Zhou, D. Yu, S. Nagase, W.-N. Mei, Z. Gao and J. Lu, *NPG Asia Mater.*, 2012, **4**, E6.
66 M. Topsakal, S. Cahangirov and S. Ciraci, *Appl. Phys. Lett.*, 2010, **96**, 091912.
67 R. N. Thurston and K. Brugger, *Phys. Rev. A*, 1964, **133**,

1604.
68 K. Brugger, *Phys. Rev. A*, 1964, **133**, 1611.
69 Y. Hiki, *Annu. Rev. Mater. Sci.*, 1981, **11**, 51.
70 K. Brugger, *J. Appl. Phys.*, 1965, **36**, 768.
71 W. B. Gauster and M. A. Breazeale, *Phys. Rev.*, 1968, **168**, 655–661.
72 H. Kobayashi and Y. Hiki, *Phys. Rev. B*, 1973, **7**, 594–601.
73 Y. Hiki, J. F. Thomas and A. V. Granato, *Phys. Rev.*, 1967, **153**, 764–771.
74 J. A. Garber and A. V. Granato, *Phys. Rev. B*, 1975, **11**, 3990–3997.
75 W. P. Mason and T. B. Bateman, *J. Acoust. Soc. Am*, 1966, **40**, 852.
76 J. Melngailis, A. A. Maradudin and A. Seeger, *Phys. Rev.*, 1963, **131**, 1972–1975.
77 A. D. Brailsfo, *J. Appl. Phys.*, 1972, **43**, 1380.
78 M. Wuttig and T. Suzuki, *Acta Metall.*, 1979, **27**, 755–761.
79 K. Fossheim, K. Kajimura, T. G. Kazyaka, R. L. Melcher and N. S. Shiren, *Phys. Rev. B*, 1978, **17**, 964–998.
80 C. Lee, X. Wei, J. W. Kysar and J. Hone, *Science*, 2008, **321**, 385–388.
81 X. Wei, B. Fragneaud, C. A. Marianetti and J. W. Kysar, *Phys. Rev. B*, 2009, **80**, 205407.
82 M. Topsakal, E. Aktürk and S. Ciraci, *Phys. Rev. B*, 2009, **79**, 115442.
83 F. Everest, *The Master Handbook of Acoustics*, McGraw-Hill, New York, 2001.
84 D. G. Kipshidze, H. P. Schenk, A. Fissel, U. Kaiser, J. Schulze, W. Richter, M. Weihnacht, R. Kunze and J. Krausslich, *Semiconductors*, 1999, **33**, 1241–1246.
85 E. R. Benes, R. Groschl, F. Seifert and A. Pohl, *IEEE Transactions On Ultrasonics Ferroelectrics And Frequency Control*, 1998, **45**, 1314–1330.
86 R. Weigel, D. P. Morgan, J. M. Owens, A. Ballato, K. M. Lakin, K. Hashimoto and C. C. W. Ruppel, *Microwave Theory and Techniques, IEEE Transactions on*, 2002, **50**, 738–749.